IOPscience iopscience.iop.org

Home Search Collections Journals About Contact us My IOPscience

Self-organized bimetallic Ag–Co nanoparticles with tunable localized surface plasmons showing high environmental stability and sensitivity

This article has been downloaded from IOPscience. Please scroll down to see the full text article.

2012 Nanotechnology 23 275604

(http://iopscience.iop.org/0957-4484/23/27/275604)

View the table of contents for this issue, or go to the journal homepage for more

Download details:
IP Address: 96.60.251.2
The article was downloaded on 20/06/2012 at 02:11

Please note that terms and conditions apply.

Nanotechnology **23** (2012) 275604 (8pp) doi:10.1088/0957-4484/23/27/275604

Self-organized bimetallic Ag–Co nanoparticles with tunable localized surface plasmons showing high environmental stability and sensitivity

R Sachan[1], S Yadavali[2], N Shirato[1], H Krishna[3], V Ramos[1], G Duscher[1,4], S J Pennycook[1,4], A K Gangopadhyay[3], H Garcia[5] and R Kalyanaraman[1,2]

[1] Department of Materials Science and Engineering, University of Tennessee, Knoxville, TN 37996, USA
[2] Department of Chemical and Biomolecular Engineering, University of Tennessee, Knoxville, TN 37996, USA
[3] Department of Physics and Center for Materials Innovation, Washington University in St Louis, MO 63130, USA
[4] Material Science and Technology Division, Oak Ridge National Laboratory, Oak Ridge, TN 37831, USA
[5] Department of Physics, Southern Illinois University, Edwardsville, IL 62026, USA

E-mail: ramki@utk.edu

Received 28 March 2012, in final form 2 May 2012
Published 19 June 2012
Online at stacks.iop.org/Nano/23/275604

Abstract
We demonstrate a promising synthesis route based on pulsed laser dewetting of bilayer films (Ag and Co) to make bimetallic nanoparticle arrays. By combining experiment and theory we establish a parameter space for the independent control of composition and diameter for the bimetallic nanoparticles. As a result, physical properties, such as the localized surface plasmon resonance (LSPR), that depend on particle size and composition can be readily tuned over a wavelength range one order of magnitude greater than for pure Ag nanoparticles. The LSPR detection sensitivity of the bimetallic nanoparticles with narrow size distribution was found to be high—comparable with pure Ag (∼60 nm/RIU). Moreover, they showed significantly higher long-term environmental stability over pure Ag.

(Some figures may appear in colour only in the online journal)

1. Introduction

Innovative and cost-effective nanomaterials which improve upon or introduce new functionalities within small dimensions are seen as a driving force for technological advancement [1]. One such category of nanomaterials is bimetallic systems made by combining immiscible metals of different functional properties [2]. Besides their potential applications as sensing and therapeutic materials [3, 4], their multifunctional properties, such as ferromagnetic–plasmonic behavior, can accelerate detection rates of superparamagnetically-tagged molecules [5], enable chemical sensing through magneto-optics [6, 7], and potentially improve high-speed optical communication circuits and energy harvesting devices [8, 9]. Another advantage of bimetallic nanomaterials, besides their physical properties, could be the unique chemical and/or environmental behavior due to the proximity of different materials [10]. For instance, bimetallic catalysts show different catalytic properties as compared to the pure components [11, 12].

With the obvious potential benefits of bimetallic nanoparticles in mind, we have addressed several outstanding issues in this work. The first is the challenge in making

 © 2012 IOP Publishing Ltd Printed in the UK & the USA

such materials in a simple and cost-effective manner. Existing synthesis procedures to create bimetallic nanoparticles are primary chemical synthesis routes that, while reasonably successful, are limited by their use of toxic and non-toxic chemicals and associated waste [2, 11, 13, 14]. Synthesis routes based on vapor phase or physical vapor deposition techniques have, as yet, not shown the range of composition, size, and array formation control that would make them useful as synthesis routes for surface arrays [15–17]. On the other hand, synthesis routes based on dewetting of thin films, such as e-beam induced dewetting [18], thermal annealing [19] and microwave plasma assisted dewetting [20], have considered nanoparticle array formation primarily focused towards plasmon-based applications. However, the ability to create bimetallic nanoparticles with a controlled size and composition has not been reported in any of these processes. Recently, a cost-effective synthesis of multimetallic nanomaterials has been demonstrated using the technique of nanosecond pulsed laser dewetting of ultrathin bilayer films [21]. More importantly, theoretical modeling studies have shown that such nanomaterials may inherit a rich variety of compositional structures within the nanoparticles if the starting metals are immiscible [22]. Here, we have utilized this laser technique for a model system comprised of Ag and Co films on SiO_2 surfaces, chosen for several reasons. First, as Ag and Co have negligible miscibility in the liquid and solid states, the resulting nanoparticles are expected to be spatially segregated. Second, the two metals have strong plasmonic (Ag) and ferromagnetic (Co) properties, making them useful candidates for multifunctional applications. Third, the contrasting oxidation tendencies of Ag and Co based on the standard electrochemical potential favor the formation of CoO over Ag_2O [23]. Therefore, proximity of Co and Ag within bimetallic nanostructures could reduce the degradation of Ag, thus permitting more environmentally stable Ag plasmon behavior.

In this work, we first present investigations of the synthesis of bimetallic nanoparticles resulting from pulsed laser dewetting of bilayer films of varying thickness and arrangement ($Ag/Co/SiO_2$ and $Co/Ag/SiO_2$). Specifically their size, composition, and structure were studied by high-resolution transmission electron microscopy (HRTEM), x-ray mapping via scanning electron microscopy (SEM), and electron energy-loss spectroscopy (EELS). The relationship between the size of the bimetallic nanoparticles and the total thickness of the bilayer, as well as the order of arrangement of the bilayers, was obtained, while the composition of the nanoparticles was evaluated in terms of the thickness ratio. The experimental findings were combined with self-organization theory to establish the parameter space for independent control of particle size and composition. We also determined the localized surface plasmon wavelength as a function of composition and size, then compared it to that of pure Ag nanoparticles of similar size. To assess the relevance of such materials in biosensing applications, we measured the sensitivity towards refractive index change of the surrounding medium for various bimetallic nanoparticle arrays and compared it to pure Ag. Lastly, the resistance towards oxidation was evidenced by measuring optical spectra of samples stored under ambient conditions over 50 days.

2. Experimental details

In the present study, thin films (1–10 nm) of Co and Ag were deposited on commercially available optical quality $SiO_2/Si(100)$ wafers consisting of a 400 nm thick thermally grown oxide layer on polished Si, using electron beam evaporation (e-beam) and pulsed laser deposition (PLD) techniques under ultrahigh vacuum. This combination of metals was chosen so as to integrate the well-known plasmonic response of Ag and the ferromagnetic properties of Co. The extremely low solid solubility ($<1\%$) of Co in Ag, and almost no solubility of Ag in Co, also help in retaining their individual functional properties in the bimetallic nanoparticles [24]. The verification of thicknesses and roughness of the deposited thin films have been done by means of atomic force microscopy (AFM). The PLD and e-beam evaporation rates for Ag and Co were calibrated for various input settings by doing step height measurements in AFM. In addition, one extra piece of substrate was kept with partial masking during every run of deposition for thickness measurements. The roughnesses of various films were also measurement by AFM and an upper limit of 0.1 ± 0.03 nm was established for the average rms roughness over the areas that were subsequently utilized in the studies [25]. Following deposition, the final stable arrays of nanoparticles were produced by irradiation at normal incidence to the substrate under vacuum with a Gaussian shaped pulsed laser beam from a neodymium-doped yttrium aluminum garnet (Nd-YAG) laser, operating at its fourth harmonic of 266 nm wavelength, with pulse width of 9 ns and repetition rate of 50 Hz. The schematic of the irradiation process has been reported earlier in [22]. The average laser energy density was chosen (between 80 and 100 mJ cm^{-2}) such that the entire bilayer could be melted for all the thickness combinations, as evidenced by a morphology change [26]. The bilayer films were irradiated for a total of 10 000 laser pulses ($\sim$2 min) to ensure the formation of nanoparticle arrays. The resulting patterns were characterized using a Hitachi S-4300 SEM operating at 15 kV. The average size of the nanoparticles was estimated from the size distribution histogram generated from the SEM images. Furthermore, the average spatial separation of the nanoparticles was obtained by analyzing the fast Fourier transform (FFT) of the SEM images. The composition and elemental distribution characteristics of the nanoparticles were obtained by x-ray mapping in SEM (JEOL JSM—7001 FLV field emission) operating at 20 kV. The crystalline structure and elemental distribution in selected samples were further examined by high-angle annular dark field imaging (HAADF) and electron energy-loss spectroscopy (EELS) in a third-order aberration corrected scanning transmission electron microscope (STEM, VG HB501UX) operating at 100 kV. The cross-sectional view TEM samples were prepared by mechanical polishing, followed by ion milling. Mechanical polishing was done by using the Multiprep system from Allied High Tech Products Inc. to thin down the samples down to 25 μm thickness. Further processing was done by twin-jet

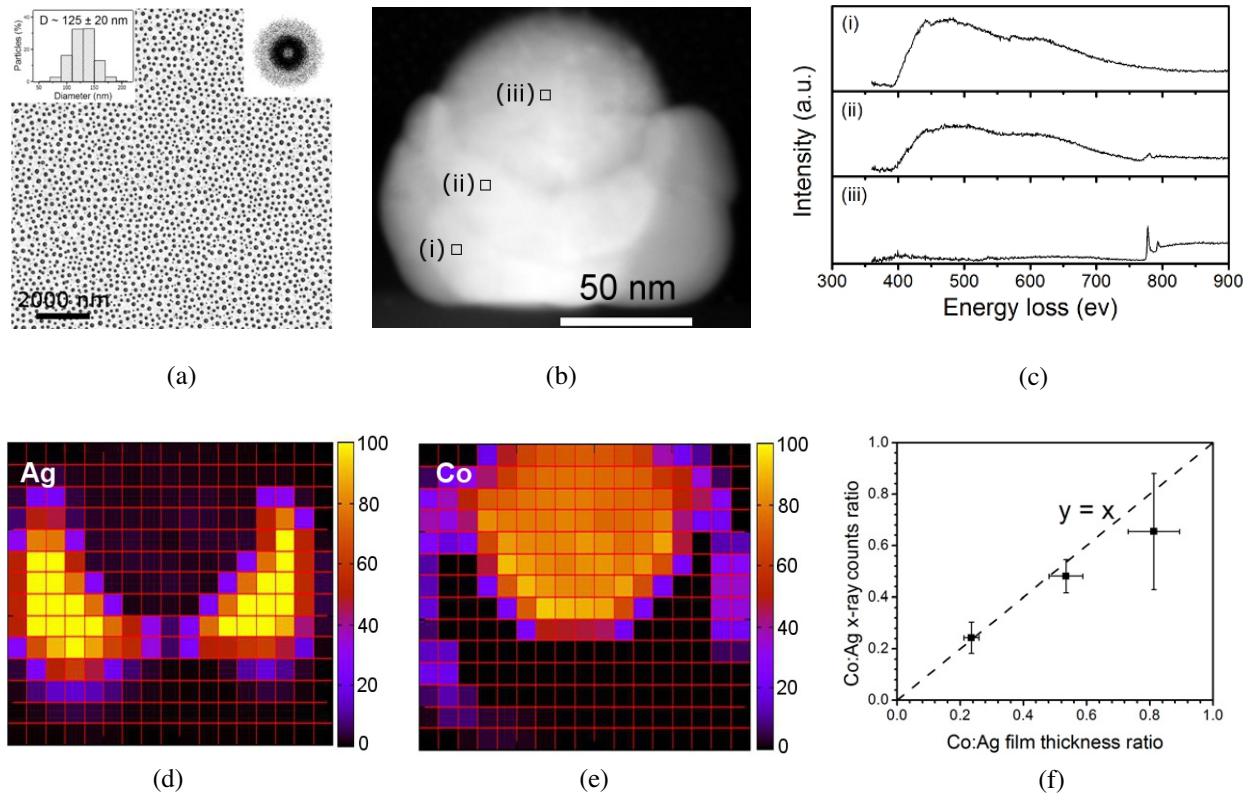

Figure 1. (a) A typical SEM micrograph showing the arrangement of nanoparticles following bilayer self-organization from the Co (5 nm)/Ag (5 nm)/SiO_2 bilayer. The histogram in the inset shows the narrow size distribution of particles achieved by this process. The FFT image in the inset shows the spatial short range ordering between the nanoparticles. (b) Cross-sectional HAADF image of a nearly hemispherical shaped Ag–Co nanoparticle made from the Co (5 nm)/Ag (5 nm)/SiO_2 bilayer showing contrast variation indicating polycrystallinity within the particle. (c) Background subtracted EELS spectra at different regions of the nanoparticle in (b), showing delayed Ag $M_{4,5}$ edge energy at 394 eV and Co L_3 edge energy at 779 eV. (d) Ag and (e) Co EELS compositional maps of the enclosed region shown in image (b), exhibiting the immiscibility of Co and Ag in each other. The step size of the compositional map is 5.9 nm × 5.9 nm. The contrast bar shows the variation of atom % of Ag and Co individually in different locations of enclosed region of image (b). (f) The average Co:Ag ratio in each nanoparticle from x-ray mapping (symbols) plotted against the Co:Ag film thickness ratio.

ion milling in Gatan's precision ion polishing system (PIPS) to make sufficiently thin (50–100 nm) samples for the TEM and EELS studies. The optical properties in the range of 250–800 nm for the various Ag–Co bimetallic particle arrays were measured by an HR2000 + ES spectrometer from Ocean Optics in the transmission mode. It required preparation of all samples on quartz substrates. For the external medium refractive index sensitivity measurements, the optical spectra were taken in air (RI = 1.00), isopropenol (RI = 1.378) and glycerol (RI = 1.47).

3. Results and discussion

3.1. Nanoparticle size, structure, and composition

The bimetallic nanoparticles arrays were first prepared by self-organization under pulsed laser melting of bilayer films with varying combinations of thickness and arrangement of Ag and Co on SiO_2. In a manner conceptually similar to the dewetting of single layer metal films under repeated melting by laser pulses [25–27], the initially flat bilayer liquid film evolves by surface perturbations having characteristic wavelengths that eventually lead to film rupture, which under continued laser pulsing results in ripening of the morphology into the final droplet state. Due to the large cooling rates under the nanosecond laser pulses, the droplets get quenched into the bimetallic nanoparticles, which were subsequently investigated here [21]. The average particle size of the arrays were analyzed by scanning electron microscopy (SEM). Figure 1(a) shows the scanning electron micrograph of a typical nanoparticle array, synthesized from the dewetting of the Co (5 nm)/Ag (5 nm)/SiO_2 bilayer system. The inset shows the particle size histogram, typifying the 'narrow size distribution' (as defined in [11]) achieved by this process. Also shown in the inset is the fast Fourier transform (FFT) of the contrast in the image. The annular ring evident in the FFT is indicative of a spatial short range order in the nearest-neighbor spacing between the nanoparticles, consistent with the dewetting self-organizing process [21]. From such SEM images, the average diameter of the particles in an array was established.

The structure and composition of the individual nanoparticles was analyzed using transmission electron microscopy (TEM) and electron energy-loss spectroscopy (EELS) measurements. A representative cross-sectional high-angle annular dark field (HAADF) image of a ∼100 nm nanoparticle obtained from dewetting of the Co (5 nm)/Ag

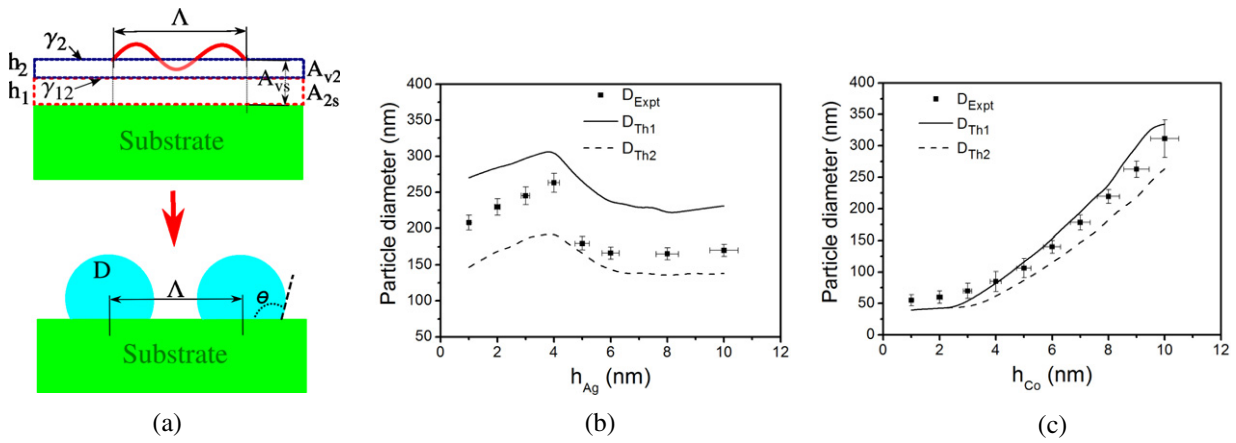

(a) (b) (c)

Figure 2. (a) Geometry of the initial bilayer film comprised of metal films of thickness h_1 and h_2. Self-organization with a characteristic deformation wavelength of Λ leads to the formation of nanoparticles of diameter D and contact angle θ. (b), (c) Comparison of the experimentally measured diameter (symbols) versus the theory predictions (lines) for the (b) $Ag/Co/SiO_2$ and (c) $Co/Ag/SiO_2$ bilayer systems. The two theory lines correspond to the bounds of theoretical Hamaker coefficient values [21].

(5 nm) bilayer on a SiO_2 substrate is shown in figure 1(b). As is evident, the nanoparticle contains several grains. The representative background subtracted EELS spectra corresponding to different regions in figure 1(b) are shown in figure 1(c). EELS spectra show the presence of (i) pure Ag, (ii) co-existence of Ag and Co and (iii) pure Co in different regions respectively. The spectra showed a delayed Ag $M_{4,5}$ edge at 394 eV and Co L_3 edge at 779 eV. The spectrum from the co-existence regions of Ag and Co (figure 1(c)-(ii)) showed no shift in Ag and Co edge energies with respect to pure Ag and Co, respectively. This indicated that Ag and Co are clearly phase segregated within the nanoparticles, as expected from the equilibrium thermodynamic phase diagram, and the mixed spectrum originated from overlapping of grains of Ag and Co along the electron beam path at this location. Figures 1(d) and (e) show the elemental distribution of Ag and Co respectively, inside the particle, analyzed by EELS near the $M_{4,5}$ edge of Ag and L_3 edge of Co. The contrast bars in figures 1(d) and (e) represent the atomic % of Ag and Co at different regions (square blocks) of the nanoparticle. From this analysis, it is once again clear that Ag and Co are spatially segregated within the nanoparticle. The EELS analysis confirmed negligible presence of oxygen in the Ag rich region.

To confirm the chemical composition of each particle in the array, SEM x-ray spatial maps (not shown here) of Ag and Co were obtained for each nanoparticle prepared from films of various ratios. From these maps, two important features were confirmed. Each nanoparticle in the map was found to consist of both Ag and Co, and the ratio of Ag/Co for each individual particle could be estimated. In figure 1(f), the closed symbols represent the value of this ratio averaged over approximately 30 particles for each composition. The y-axis error bar represents one standard deviation from this average. The good agreement with the straight line of slope = 1 indicates that, on average, each particle in the array has the same metal ratio as in the bilayer film thickness. Consequently, we conclude that the behavior of D versus concentration was identical to the D versus film thickness ratio. This is a very useful result, as it implies that the composition of a nanoparticle under dewetting self-organization of the bilayer is directly controlled by the individual film thickness.

3.2. Parameter space for independent size and composition control

Previous work on bilayer dewetting self-organization was primarily focused on the length scales of patterns formed in polymer or metallic systems [21, 28]. In recent metal bilayer work, it was shown theoretically that the characteristic self-organized length scale Λ, which described the inter-particle spacing, is a function of the material parameters and the individual film thicknesses [21]. Specifically, with respect to figure 2(a), the length scale depended on two sets of quantities. One is the intrinsic materials parameter set, which consisted of the interfacial tensions γ_2 and γ_{12}, the viscosities of the two liquids η_1 and η_2, and the Hamaker coefficients characterizing the intermolecular interactions between each pair of interfaces, i.e. vacuum–substrate (A_{vs}), vacuum–middle (A_{v2}), and middle–substrate (A_{2s}). The other was the experimentally controllable external parameters, which included the individual film thicknesses of the bilayers, h_1 and h_2, and their order of arrangement, o, on the substrate (e.g. Ag/Co versus Co/Ag). Consequently, the length scale could be expressed as a function of these variables as $\Lambda = f(\gamma, A, h, o)$.

We have estimated the dewetting length scale Λ of the bilayer system as a function of the experimentally controllable parameters o and h_i. Once Λ is known, volume conservation arguments could be used to estimate the theoretical particle diameter, D [25]. As shown in figure 2(a), the volume of an individual particle corresponds to the volume of a disc of diameter Λ and thickness h_1+h_2. For a particle with spherical shape and contact angle θ lying on a substrate, its volume can be expressed as $\frac{f(\theta)D^3}{8}$, where $f(\theta)$ is the geometrical factor related to the contact angle the particle makes with the surface. The final diameter is obtained as:

$$D = \left[\frac{2\pi\Lambda^2(h_1+h_2)}{f(\theta)}\right]^{1/3}. \quad (1)$$

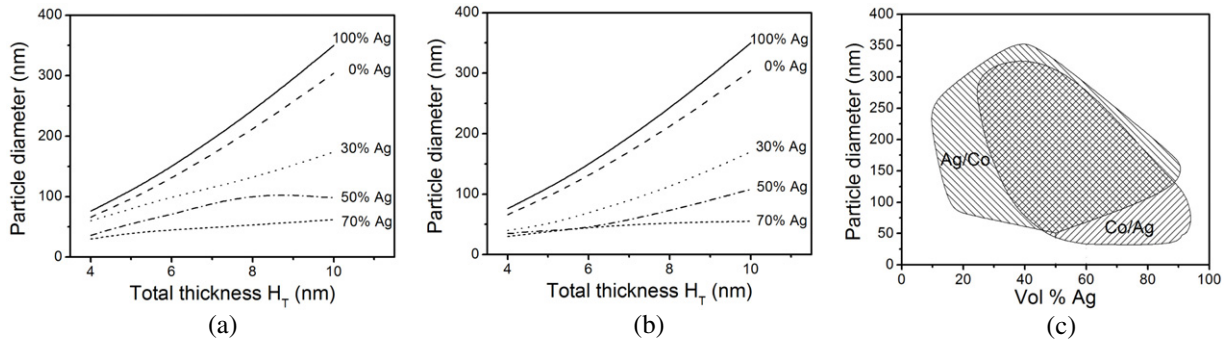

Figure 3. (a) The calculated variation of particle diameter as a function of total thickness of original bilayer films for $Ag/Co/SiO_2$. Each curve corresponds to the case of a different Ag concentration in the resulting nanoparticle. (b) Similar information as (a), but for the $Co/Ag/SiO_2$ system. The figures show that, for a given concentration, particles with large variation in size can be independently achieved. (c) The parameter space corresponding to independent control of nanoparticle diameter and composition that can be achieved by bilayer self-organization. The shaded area was generated by theoretical calculations for a range of Ag/Co and Co/Ag film thickness ratios, with total bilayer thickness ranging between 2 and 20 nm.

In figure 2, the experimentally measured diameter (symbols) is compared to the range of theoretical predictions (lines) for the Ag/Co (figure 2(b)) and Co/Ag (figure 2(c)) bilayer systems respectively, as a function of the top layer film thickness h_1; the bottom layer is kept fixed at 5 nm. The two lines correspond to the theoretical predictions based on the two different approaches to calculate the Hamaker coefficients [6, 7, 29, 30]. The A's can be calculated either from (i) summation of the frequency-dependent dielectric function of each of the layers [31], or from (ii) the various surface and interfacial energies [28]. As a result, the A values can range between 10^{-19} and 10^{-18} J. In figures 2((b) and (c)), we have estimated the theory predictions by utilizing these two values of A. The two sets of data are for fixed bottom layer (h_2) thickness of 5 nm and varying top layer thickness (∼1–10 nm) for the two cases. The theoretical contact angle, necessary to determine $f(\theta)$, was estimated from the contact angles for pure silver (θ_{Ag}) and pure Co (θ_{Co}) and their volume fractions, using $\theta = v_{Ag}\theta_{Ag} + v_{Co}\theta_{Co}$, where $\theta_{Ag} = 82°$, $\theta_{Co} = 102°$ [32], $v_{Co} = \frac{h_{Co}}{h_{Ag}+h_{Co}}$ and $v_{Ag} = \frac{h_{Ag}}{h_{Ag}+h_{Co}}$.

As evident from figures 2(b) and (c), there is good agreement between the experimental data and theoretical predictions. The significantly different behavior for the two bilayer arrangements is a direct consequence of the difference in intermolecular dispersion forces for the two configurations [21]. Such good agreement allowed us to extend the theoretical calculations for D beyond the limited experimental data, as shown in figures 3(a) and (b). The theoretical calculations for D were done for various combinations of film thickness for the Ag/Co (figure 3(a)) and Co/Ag (figure 3(b)) bilayer systems. These plots show that for a given volume composition, the nanoparticle size can be different, depending on the thickness of the thin film layers. In addition, the range of achievable particle size can be extended by changing the order of Ag–Co film arrangement. To emphasize this point further, the theoretical diameter range accessible over the whole composition range shown in figures 3(a) and (b), is combined together and described as the parameter space, as shown in figure 3(c). This figure emphasizes that the diameter for the bimetallic nanoparticles for a given composition can be varied by up to one order of magnitude over a large fraction of the composition axis, suggesting that this technique can independently control the chemical composition and size of the nanoparticles over a wide range.

3.3. Tunability of LSPR wavelength

Noble metal nanoparticles, such as of Ag or Au, show strong LSPR characteristics under optical irradiation. The spectral position of the LSPR is of fundamental interest to applications related to plasmon-based sensing and surface enhanced Raman scattering. Here, the absorbance as a function of wavelength (250–800 nm) for nanoparticle arrays with different average particle diameter (75, 90 and 105 nm) was measured. The representative optical spectra of average 90 nm nanoparticle arrays is shown in figure 4(a) for various Ag–Co compositions. In the absorbance plots, a minima is observed at ∼325 nm wavelength, which corresponds to the characteristic response of Ag due to interband transitions. Another common feature is an inflection in all the absorbance plots at ∼390 nm, which is attributed to the quadrupolar resonance effect within the bimetallic nanoparticle. LSPR peaks (λ_{LSPR}) for arrays with nanoparticles of 90 nm average diameter are observed at 440, 488 and 503 nm wavelengths for pure Ag, 82.3% Ag and 71.5% Ag respectively. In figure 4(b), λ_{LSPR} peaks are shown as a function of Ag concentration for different sized particles. As the concentration of Ag decreased, the λ_{LSPR} showed increasing red-shift. Similarly, the λ_{LSPR} red-shifted with increasing particle size for a fixed composition of the nanoparticles, as shown in figure 4(c). The important conclusion here is that Ag–Co bimetallic nanoparticles show a large tunability in the position of the λ_{LSPR} (∼200 nm), compared to only about 20 nm for pure Ag particles of identical shape and size.

To understand the LSPR shift with composition and size of nanoparticles, we have utilized an effective medium approach [33, 34] to calculate the theoretical optical-plasmonic response of these bimetallic nanoparticle arrays.

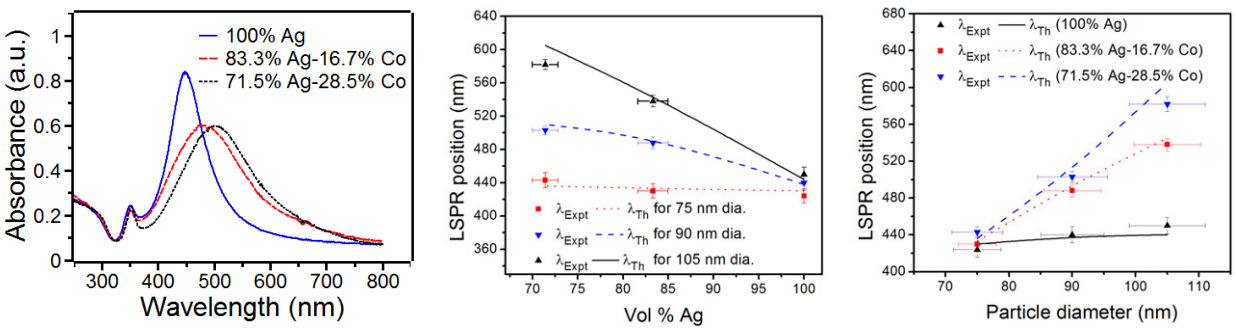

(a) (b) (c)

Figure 4. (a) LSPR position as a function of Ag–Co composition for nanoparticle arrays with similar average particle size of ∼90 nm. (b) Comparison of experimental LSPR positions (symbols) with theory predictions (lines) as a function of % Ag in nanoparticle arrays for the different average particle sizes. (c) Comparison of experimental LSPR positions (symbols) with theory predictions (lines) as a function of nanoparticle size for various particle compositions based on modeling results [33].

When the diameter D of a nanoparticle is less than the wavelength λ of light, such as in the present work, the optical response can be expressed as coming from a homogeneous medium with an effective dielectric function ϵ_{eff}. Using the Maxwell–Garnett (MG) approach, the ϵ_{NP} for a nanoparticle made by grains of material 1 embedded randomly in a medium of type 2 can be expressed as:

$$\epsilon_{\text{NP}} = \epsilon_2 + \frac{3f\epsilon_2(\epsilon_1 - \epsilon_2)}{\epsilon_1 + 2\epsilon_2 - f(\epsilon_1 - \epsilon_2)} \quad (2)$$

where ϵ_1 and ϵ_2 are the complex dielectric permittivities of material 1 and 2 (here Ag and Co), and f is the volume fraction of material 1 in 2. Then, the optical response of the nanoparticle array is modeled as a layer of thickness $D/2$ made from hemispherical particles of average diameter D consisting of grains of Co and Ag, and embedded in a host medium of effective dielectric function ϵ_{host}, which is made from air and SiO_2 [35] (figure 2(a)). The effective dielectric function of the host medium is given by $\epsilon_{\text{host}} = \epsilon_{\text{SiO2}}\sigma + (1-\sigma)\epsilon_{\text{air}}$, where the subscripts refer to the dielectric of the substrate and surrounding materials, and σ is the fraction of the nanoparticle area in contact with the substrate. For the case of hemispherical particles, σ is 0.33. In the final step, the MG mixing model of equation (2) was applied self-consistently to obtain the final dielectric function, with ϵ_{NP} and ϵ_{host} replacing ϵ_1 and ϵ_2 in equation (2) and the volume fraction of particles given by $f = \frac{2\pi}{3}(\frac{D}{2\Lambda})^2$. From these calculations, the theoretical optical transmission data was generated, as in [35], and the location of the LSPR was obtained from the minimum in the transmission plot. The grain sizes within the nanoparticles were assumed to be 5–10 nm, which is not far off from the experimental observations. However, it was found theoretically that the size of the individual grains of the two metals did not have a strong influence on the overall LSPR position. In figures 4((b) and (c)), the theoretically estimated LSPR position (lines) from this model is compared with the experimental data (symbols). Excellent agreement is seen with experiment, including prediction of the different magnitudes of the red-shifts for the different sized particles. This result suggested that the observation of figures 4(a)–(c) is a direct result of the size, shape, composition, and spacing of the nanoparticles, which are the only experimental parameters in the model.

3.4. LSPR-based sensing

One of the most important aspects of selecting plasmonic materials for sensing applications is its sensitivity towards refractive index change of the external environment. Sensitivity is defined as the rate of change in LSPR wavelength with refractive index, usually in units of nm/RIU. In figure 5(a), variation in the λ_{LSPR} as a function of refractive index of external dielectric environment is presented for various sizes and compositions of pure Ag and bimetallic Ag–Co nanoparticle arrays. The external dielectric was varied by encapsulating the samples in fluids with different refractive index, as described in section 2. As evident from the plot, the LSPR shift is linearly dependent on the refractive index of the ambient environment. Ag–Co particle arrays show sensitivities of 51 and 71 nm/RIU respectively for 90 nm sized nanoparticles with composition of 83.3% Ag and 71.5% Ag, whereas 110 nm sized Ag–Co particle arrays show sensitivities of 105 and 56 nm/RIU for the 83.3% Ag and 71.5% Ag compositions. Also shown by the square symbols are similar measurements made using pure Ag nanoparticle arrays with particle sizes of 90 (solid square) and 100 nm (open square), which show sensitivities of 62 and 60 nm/RIU respectively. These measurements indicated that the sensitivity of the Ag–Co bimetallic arrays, which ranged between 51 and 105 nm/RIU, was similar or comparable to pure Ag particles of similar shape and size despite the bimetallic particles having a broader LSPR peak as compared to pure Ag (figure 4(a)).

As is well known, Ag oxidizes rapidly, and the associated changes to its surface and optical-plasmonic properties limit its use when long-term stable behavior is required [36–39]. As was mentioned previously, (section 3.1), TEM EELS results showed the negligible presence of oxygen in the Ag–Co nanoparticles, such as the ones in figures 1(d) and (e), implying that Ag oxidation is suppressed. To further

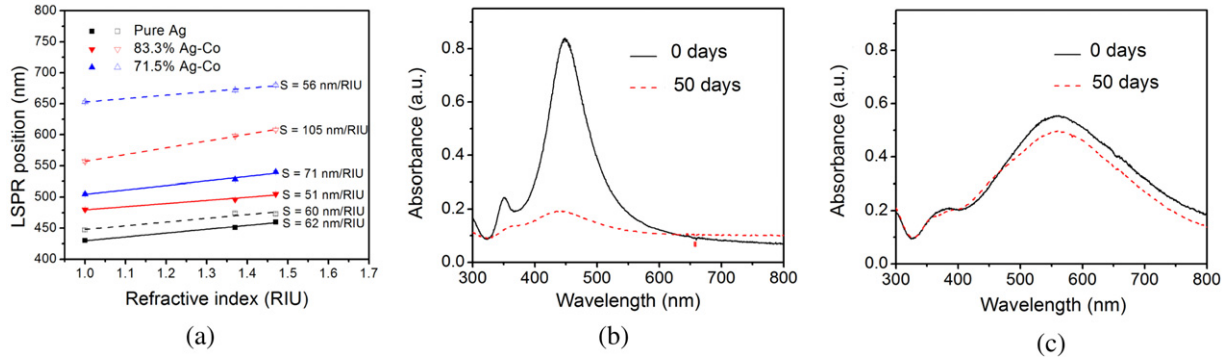

Figure 5. (a) The shift in LSPR peak position as a function of refractive index (RI) of the external medium for various nanoparticle arrays. The plot shows the linear dependence of LSPR shift w.r.t. RI of external environment. Also, the slope depicts the sensitivity (in nm/RIU) of the respective nanoparticle arrays. The solid scatter points correspond to arrays with average particle size of 90 nm while open scatter points are for 110 nm. (b) The optical absorbance of 105 nm sized pure Ag sample, taken immediately after synthesizing the sample and following a 50-day interval. (c) The optical absorbance spectra of 105 nm sized 83.3% Ag–Co sample, taken immediately after synthesizing the sample and after a 50-day interval.

demonstrate this apparent stability to oxidation, we measured the optical transmission spectra of pure Ag and 83.3% Ag–Co nanoparticle arrays (both with average particle size of ∼105 nm) over 50-day intervals, as shown in figures 5(b) and (c) respectively. The samples were stored under ambient conditions of temperature and indoor humidity over the 50-day period. It is clear that Ag nanoparticles showed a drastic degradation in the LSPR quality as compared to similar sized 83.3% Ag–Co nanoparticles. While a detailed understanding of this property of the Ag–Co particles is unclear, it is quite likely that the higher electrochemical and thermodynamic oxidation tendency of Co over Ag could be responsible for the suppression of Ag oxidation. The two metals have contrasting oxidation tendencies, as seen from their standard state electrochemical oxidation potentials (0.28 eV and −0.7996 eV for Co and Ag, respectively). As can be noted from the Ellingham diagram, the formation of CoO is favored over that of Ag_2O [23]. Therefore, it is quite likely that the proximity of Co and Ag within bimetallic nanostructures could reduce the degradation of Ag, thus permitting more environmentally stable Ag plasmon behavior. The results presented here suggest that the bimetallic particles can potentially be useful in applications which require flexibility in tuning the LSPR wavelength, and/or in applications requiring high LSPR sensitivity with a long-term stability of the material to oxidation.

4. Conclusion

We have presented a route based on nanosecond pulsed laser dewetting and self-organization of ultrathin bilayer metallic films to synthesize bimetallic nanoparticles. As a model system, we have investigated bilayers of Co and Ag metal on SiO_2 substrates. The particle size was uniquely controlled by the individual film thickness and their order of arrangement on the substrate. X-ray mapping and electron energy-loss spectroscopy helped confirm that the individual nanoparticles are bimetallics of phase-separated Co and Ag nanograins in the same compositional ratio as in the starting films. By utilizing self-organization theory, a large parameter space for independent control of particle size and composition was established for this technique. We demonstrated that the nanoparticle size could be changed independently by one order of magnitude (∼25–350 nm), and composition by 85% (from 10 to 95% of Ag). As a result, large and predictable tunability in the physical properties is feasible, as demonstrated for the localized surface plasmon resonance in this Ag–Co system. The LSPR wavelength could be tuned over ∼200 nm as a function of size and/or composition of the bimetallic nanoparticles, compared to only ∼20 nm for pure Ag. We also established that the bimetallic arrays have a refractive index sensitivity that is comparable to that of pure Ag arrays. In addition, the bimetallic system showed significantly higher stability against environmental degradation of the LSPR signal as compared to pure Ag. These studies established two key findings. First, with judicious choice of film thickness and bilayer arrangement, dewetting by nanosecond pulsed laser melting represents a simple and cost-effective method to synthesize novel bimetallic nanomaterials with tunable properties. Second, the plasmonic behaviors evidenced here for the Ag–Co bimetallic nanoparticle arrays suggest that they can potentially be useful for broadband scattering and solar light trapping applications due to the flexibility in tuning the LSPR wavelength, and in LSPR or surface enhanced Raman sensing applications which require high LSPR sensitivity with a long-term stability of the material to oxidation. Future work will be directed towards understanding and utilizing the coupling of the different properties of the two metals (plasmonic and ferromagnetic in the present bimetallic system) so that new functional properties of the nanomaterials may be achieved.

Acknowledgments

The authors acknowledge support by the Sustainable Energy Education and Research Center, Center for Materials Innovation, Center for Materials Processing, TN-SCORE, and by the NSF through grants CMMI-0855949 and DMR-0856707. Authors also acknowledge the US Department of

Energy grant DE-FG02-84DR45170 for using STEM facility in ORNL.

References

[1] Vollath D 2010 Bifunctional nanocomposites with magnetic and luminescence properties *Adv. Mater.* **22** 4410–5

[2] Wang D and Li Y 2011 Bimetallic nanocrystals: liquid-phase synthesis and catalytic applications *Adv. Mater.* **23** 1044–60

[3] Peng S, Lei C, Ren Y, Cook R and Sun Y 2011 Plasmonic/magnetic bifunctional nanoparticles *Angew. Chem.* **50** 3158–63

[4] Chen W, Xu N, Xu L, Wang L, Li Z, Ma W, Zhu Y, Xu C and Kotov N 2010 Multifunctional magnetoplasmonic nanoparticle assemblies for cancer therapy and diagnostics (theranostics) *Macromol. Rapid Commun.* **31** 228–36

[5] Wang Y, Dosalek J and Knoll W 2010 Magnetic nanoparticle-enhanced SPR biosensor *Proc. Eng.* **5** 1017–20

[6] Sepúlveda B, Calle A, Lechuga L M and Armelles G 2006 Highly sensitive detection of biomolecules with the magneto-optic surface-plasmon-resonance sensor *Opt. Lett.* **31** 1085

[7] Newman D M, Matelon R J, Wears M L and Savage L B 2010 The *in vivo* diagnosis of malaria: feasibility study into a magneto-optic fingertip probe *IEEE J. Sel Top. Quantum Electron.* **16** 573–80

[8] Schaadt D M, Feng B and Yu E T 2005 Enhanced semiconductor optical absorption via surface plasmon excitation in metal nanoparticles *Appl. Phys. Lett.* **86** 063106

[9] Shoji Y, Mizumoto T, Yokoi H, Hsieh I-W and Osgood R M Jr 2008 Magneto-optical isolator with silicon waveguides fabricated by direct bonding *Appl. Phys. Lett.* **92** 07117

[10] Ng K, Liu H and Penner R 2000 Subnanometer silver clusters exhibiting unexpected electrochemical metastability on graphite *Langmuir* **16** 4016–23

[11] Bonnemann H and Richards R 2001 Nanoscopic metal particles—synthetic methods and potential applications *Eur. J. Inorg. Chem.* **2001** 2455–80

[12] Luo J, Maye M, Petkov V, Kariuki N, Wang L, Njoki P, Mott D, Lln Y and Zhong C 2005 Phase properties of carbon-supported gold–platinum nanoparticles with different bimetallic compositions *Chem. Mater.* **17** 3086–91

[13] Cable R and Schaak R 2005 Low-temperature solution synthesis of nanocrystalline binary intermetallic compounds using the polyol process *Chem. Mater.* **17** 6835–41

[14] Pazos-Perez N, Gao Y, Hilgendorff M, Irsen S, Pereez-Juste J, Spasova M, Farle M, Liz-Marzan L M and Giersig M 2007 Magnetic-noble metal nanocomposites with morphology-dependent optical response *Chem. Mater.* **19** 4415–22

[15] Yang K, Clavero C, Skuza J R, Varela M and Lukaszew R A 2010 Surface plasmon resonance and magneto-optical enhancement on Au–Co nanocomposite thin films *J. Appl. Phys.* **107** 103924

[16] Safarov V I, Kosobukin V A, Hermann C, Lampel G, Peretti J and Marlière C 1994 Magneto-optical effects enhanced by surface plasmons in metallic multilayer films *Phys. Rev. Lett.* **73** 3584–7

[17] Guillot N, Shen H, Frémaux B, Péron O, Rinnert E, Toury T and Lamy de la Chapelle M 2010 Surface enhanced Raman scattering optimization of gold nanocylinder arrays: influence of the localized surface plasmon resonance and excitation wavelength *Appl. Phys. Lett.* **97** 023113

[18] Yasuhiko K Y and Kato T 2008 Nanoparticle formation in Au thin films by electron-beam-induced dewetting *Nanotechnology* **19** 255605

[19] Liao T, Lee B, Lee C and Wei P 2011 Large-area Raman enhancement substrates using spontaneous dewetting of gold films and silver nanoparticles deposition *Sensors Actuators* B **156** 245–50

[20] Hsu C, Huang J, Gwo S and Lin K 2010 The facile fabrication of tunable plasmonic gold nanostructure arrays using microwave plasma *Nanotechnology* **21** 035302

[21] Krishna H, Shirato N, Yadavali S, Sachan R, Strader J and Kalyanaraman R 2011 Self-organization of nanoscale multilayer liquid metal films: experiment and theory *ACS Nano* **5** 470–6

[22] Khenner M, Yadavali S and Kalyanaraman R 2011 Formation of organized nanostructures from unstable bilayers of thin metallic liquids *Phys. Fluids* **23** 122105

[23] Gaskell D R 2008 *Intorduction to the Thermodynamics of Materials* (London: Taylor and Francis)

[24] Massalski T B (ed) 1990 *Binary Alloy Phase Diagrams* 2nd edn (Metals Park, OH: ASM International)

[25] Trice J, Thomas D G, Favazza C, Sureshkumar R and Kalyanaraman R 2007 Investigation of pulsed laser induced dewetting in nanoscopic Co films: theory and experiments *Phys. Rev.* B **75** 235439

[26] Favazza C, Kalyanaraman R and Sureshkumar R 2006 Robust nanopatterning by laser-induced dewetting of metal nanofilms *Nanotechnology* **17** 4229–34

[27] Bischof J, Scherer D, Herminghaus S and Leiderer P 1996 Dewetting modes of thin metallic films: nucleation of holes and spinodal dewetting *Phys. Rev. Lett.* **77** 1536–9

[28] Bandyopadhyay D, Gulabani R and Sharma A 2005 Instability and dynamics of thin liquid bilayers *Ind. Eng. Chem. Res.* **44** 1259

[29] Soelberg S D, Stevens R C, Limaye A P and Furlong C E 2009 Surface plasmon resonance detection using antibody-linked magnetic nanoparticles for analyte capture, purification, concentration, and signal amplification *Anal. Chem.* **81** 2357–63

[30] Wang J, Wang L Y, Sun Y, Zhu X N, Xu H Y, Bi N, Zhang H Q, Cao Y B, Wang X H and Song D Q 2010 Preparation of core/shell Fe_3O_4/Au nanocomposite and its application to surface plasmon resonance biosensor *Acta Chim. Sin.* **68** 263–8

[31] Israelachvili J 1992 *Intermolecular and Surface Forces Chapter van der Waals Forces Between Surfaces* (London: Academic)

[32] Krishna H, Sachan R, Strader J, Favazza C, Khenner M and Kalyanaraman R 2010 Thickness-dependent spontaneous dewetting morphology of ultrathin Ag films *Nanotechnology* **21** 155601

[33] Garcia H, Trice J, Kalyanaraman R and Sureshkumar R 2007 Self consistent determination of plasmonic resonance in ternary nanocomposites *Phys. Rev.* B **75** 045439

[34] Garcia H, Kalyanaraman R and Sureshkumar R 2009 Nonlinear optical properties of multi-metal nanocomposites in a glass matrix *J. Phys. B: At. Mol. Opt. Phys.* **42** 175401

[35] Garcia H, Sachan R and Kalyanaraman R 2012 Optical plasmon properties of Co–Ag nanocomposites within the mean-field approximation *Plasmonics* **7** 137–41

[36] Lavrenko V A, Malyshevskaya A I, Kuznetsova L I, Litvinenko V F and Pavlikov V N 2006 Features of high-temperature oxidation in air of silver and alloy Ag–Cu, and adsorption of oxygen on silver *Powder Metal. Met. Ceram.* **45** 476–80

[37] Yun Han Y, Lupitskyy R, Chou T, Stafford C, Du H and Sukhishvili S 2011 Effect of oxidation on surface-enhanced Raman scattering activity of silver nanoparticles: a quantitative correlation *Anal. Chem.* **83** 5873–80

[38] Ivanova O and Zamborini F 2010 Size-dependent electrochemical oxidation of silver nanoparticles *J. Am. Chem. Soc.* **132** 70–2

[39] Cao W and Elsayed-Ali H 2009 Stability of Ag nanoparticles fabricated by electron beam lithography *Mater. Lett.* **63** 2263–6